Transactions of Materials Research 1 (2025) 100014

Contents lists available at ScienceDirect

Transactions of Materials Research

journal homepage: www.sciencedirect.com/journal/transactions-of-materials-research

Refined martensite and enhanced strength of selective laser melted Ti6.5Al2.5Zr1Mo1V matrix composites by minor nano TiBw addition

Qi An [a,b], Lihua Cui [a], Delong Gong [a], Han Cheng [a], Ying Liu [a], Rui Zhang [a], Yang Bao [a], Lujun Huang [a,b,*], Lin Geng [a,b]

[a] School of Materials Science and Engineering, Harbin Institute of Technology, Harbin, 150001, China
[b] State Key Laboratory of Precision Welding & Joining of Materials and Structures, Harbin, 150001, China

ARTICLE INFO

Keywords:
Titanium matrix composites
Selective laser melting
Minor TiBw
Microstructure evolution
Strengthening mechanisms

ABSTRACT

To achieve strength improvement while ensuring a certain degree of plasticity of titanium matrix composites (TMCs) by selective laser melting (SLM), minor TiB_2 particles were used to fabricate *in situ* TiB whiskers (TiBw) reinforced Ti6.5Al2.5Zr1Mo1V composites in this work. It is found that pore defects in the as-printed TMCs reduce with the decreasing energy density. The porosity of as-printed TMCs decreases to 0.0005% under an optimized energy density of 61 $J{\cdot}mm^{-3}$. To establish the relationship between porosity and SLM parameters, a systematic investigation of the influence of SLM parameters on the microstructure of TMCs is conducted, and the microstructure evolution is clarified during complex thermal cycling. The nano TiBw effectively hinders the coarsening of hierarchical martensite during the complex thermal cycles. As a result, the martensite plate thickness is approximately 60% in comparison with the as-printed Ti6.5Al2.5Zr1Mo1V alloy. A remarkable strengthening effect is achieved with minor TiBw, resulting in an impressive tensile strength of 1432 MPa and yield strength of 1320 MPa, while an elongation rate of 4.0% is maintained.

1. Introduction

Titanium matrix composites (TMCs) have extensive applications in aerospace, automotive, military and marine industries, as interface as in biomedical and other sectors owing to their exceptional specific strength, specific modulus, high-temperature durability, and wear resistance [1–8]. The *in situ* TiBw, one of the most popular reinforcements in TMCs, has low density, high modulus of elasticity, high tensile strength, good thermal stability and similar thermal expansion coefficient as those of titanium and titanium alloys [9–12]. The interface between the *in situ* TiBw and the matrix is well-bonded and free from reaction product [13], which enhances the overall performance of TMCs due to high thermodynamic stability.

Currently, due to the complex shape of important structural parts such as the head shells of aerospace aircraft and air rudders [14–16], the laser additive manufacturing technology has become an ideal method for fabricating metallic components with complex shapes and structures based on the near-net-shape-manufacturing capability. selective laser melting (SLM), also known as laser powder bed fusion (LPBF), is an additive manufacturing technology in the form of high energy laser beam as an energy source and powder bed as raw material [17]. In particular, SLM has the advantage of high forming accuracy due to the fine beam diameter and fine powder. In addition, the extremely rapid melting and solidification process of SLM also leads to the refinement of grains and the *in situ* synthesis of nano scale reinforcements [18]. Jiang et al. [19] prepared Ti6Al4V alloy and TiC/Ti6Al4V composite by SLM. They found that a higher energy density was always required to prepare TiC/Ti6Al4V than Ti6Al4V. A similar result was concluded by Fereiduni et al. [20] that the relative density of TMCs raised initially and then decreased with the increase of the input energy density during SLM. Liu et al. [21] prepared *in situ* TiBw/Ti6Al4V composites by SLM, disclosing the TiBw could significantly improve the strength of the material. However, the elongation was reduced from 7.7% to 2.6% significantly. Li et al. [22] fabricated TiC/Ti6Al4V with 0 vol% to 50 vol% by laser melting deposition (LMD) and observed that composites with more than 5% volume fraction of the reinforcement (TiC) would have adverse effects on their mechanical properties due to the incomplete dissolution and the brittleness of TiC.

From the current research status, some basic research has been carried out on the additive manufacturing of TMCs. Due to the incorporation

* Corresponding author. School of Materials Science and Engineering, Harbin Institute of Technology, Harbin, 150001, China.
E-mail address: huanglujun@hit.edu.cn (L. Huang).

https://doi.org/10.1016/j.tramat.2025.100014
Received 28 March 2025; Received in revised form 7 April 2025; Accepted 7 April 2025
Available online 8 April 2025

of ceramic phases, the plasticity of TMCs is consistently diminished, rendering TMCs is susceptible to cracking during the printing process. Accordingly, pure titanium or Ti6Al4V with superior plasticity is invariably employed as the matrix [23–25]. Few studies focus on near-α titanium alloys as they are prone to cracking in the process of SLM, due to low ductility induced by high Al equivalent. However, near-α type titanium alloys have excellent high-temperature performance [26]. The additive manufacturing of TMCs with near-α alloy matrix would have more potential to be applied in aerospace fields with high-temperature environments. In addition, the volume fraction of the TiBw enhancement phase needs to be designed, since high content often results in low ductility.

In this study, near-α Ti6.5Al2Zr1Mo1V alloy powder and submicron TiB_2 ceramic particles were selected as raw materials to prepare TiBw/Ti6.5Al2.5Zr1Mo1V composites by SLM. The crack-free and high-relative density TMCs were achieved by optimizing the process parameters. As a result, the tensile strength and yield strength of as-printed TMCs exhibited a significant increase compared to those of the as-printed Ti6.5Al2.5Zr1Mo1V alloy. The detailed microstructure evolution during SLM and the strengthening mechanisms of *in situ* nano-TiBw were analyzed. The study possesses a certain reference value for the research and application of additive manufacturing of TMCs.

2. Experimental procedure

2.1. Fabrication of TiBw/Ti6.5Al2.5Zr1Mo1V composites

In this work, Ti6.5Al2.5Zr1Mo1V alloy powder (Fig. 1a) with a particle size range of 15–53 μm was sourced from ZTT SRIM Additive Manufacturing Co., Ltd., while TiB_2 particles (Fig. 1b) with a particle size range of 0.5–1 μm and a purity of 99% were obtained from FORSMAN Co., Ltd. Firstly, the low-energy ball milling, with parameters defined as a rotation speed of 220 rpm, a milling duration of 5 h, balls with a diameter of 10 mm, and a ball-to-powder ratio of 2:1, was used to mix the two raw materials under argon atmosphere. The model of ball mill equipment is QM-2SP12. As shown in Fig. 1c and d, the small-sized TiB_2 particles were evenly embedded on the surface of the large-size alloy powder, and the alloy powder still maintained good sphericity after low-energy ball milling. Secondly, the composite samples were fabricated using BLT S210 SLM equipment with a fixed layer thickness of 30 μm, a hatching spacing of 90 μm, and a preheating temperature of 180 °C. The laser scanning direction between adjacent layers was rotated 67° during the preparation process. Fig. 1e shows the schematic illustration of the scanning strategy and the detailed dimensions of the mechanical property specimen. In this study, the laser power and scanning speed were varied. The influence of SLM parameters can be comprehensively described by different volume

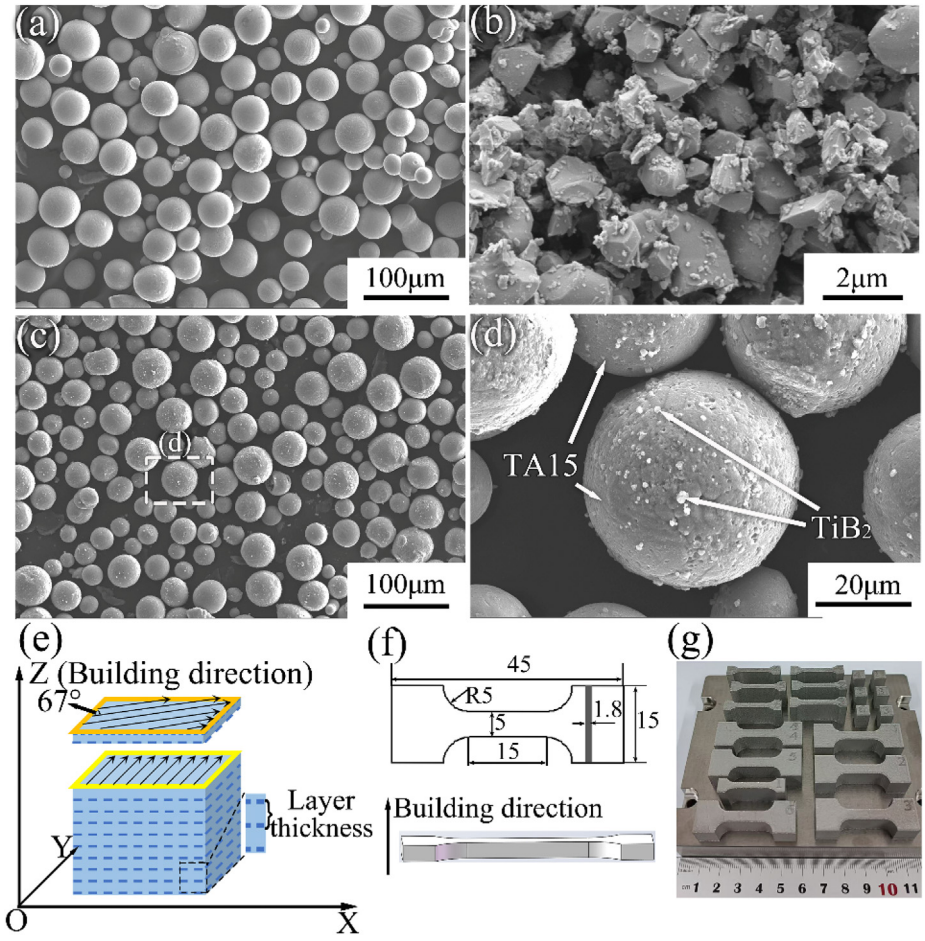

Fig. 1. SEM images of powder: (a) Ti6.5Al2.5Zr1Mo1V alloy powder (15–53 μm), (b) TiB_2 particles (0.5–1 μm), (c, d) ball-milled 0.5 wt% TiB_2/Ti6.5Al2.5Zr1Mo1V powder at low and high magnification. (e) Schematic illustration of the scanning strategy. (f) Construction orientation of the stretched samples and the detailed dimensions of mechanical properties specimen. (g) Samples prepared by SLM.

energy densities (VED). The relationship between VED and SLM parameters can be expressed as [27].

$$\mathrm{VED} = \frac{P}{v \times h \times t}, \quad (1)$$

where VED is the volume laser energy density ($J{\cdot}mm^{-3}$), P is the laser power (W), v is the scanning speed (mm/s), h is the scanning spacing (mm), t is the powder layer thickness (mm). The specific SLM parameters and corresponding VED are shown in Table S1 of the Supplementary material. The as-printed samples without macroscopic cracking indicate excellent formability (Fig. 1g).

The as-printed samples without cracks are shown in Fig. 1g. According to the relationship between the mass fraction of TiB_2 and the volume fraction of TiBw expressed in the following, 0.5 wt% TiB_2/Ti6.5Al2.5Zr1Mo1V can be transformed into 0.85 vol% TiBw/Ti6.5Al2.5Zr1Mo1V based on the chemical reaction of TiB_2+Ti→2TiB.

$$1\,\mathrm{wt.\%TiB_2} = 1.7\,\mathrm{vol.\%TiB}. \quad (2)$$

2.2. Phase constitution and microstructure characterization

The morphology of Ti6.5Al2.5Zr1Mo1V alloy, TiB_2, and mixed TiB_2/Ti6.5Al2.5Zr1Mo1V was observed with a Zeiss Gemini-300 scanning electron microscope (SEM). The transverse (XOY) and longitudinal (XOZ) cross-sections of the samples were obtained by wire-cutting electrical discharge machining. Three different locations on each cross-section were selected for porosity statistics through the software Image J and the average value was taken as the porosity of the sample. A Xradia 520 Versa three-dimensional X-ray microscopy (3D-CT) with a step size of 1 μm was used to further measure the porosity of the TMCs. The sample for 3D-CT is the cylinder with a diameter of 1 mm and a height of 2 mm. The microstructures of the TMCs after etching were observed with a JX-50M optical microscope (OM) and a Zeiss Gemini-300 SEM. The acceleration voltage of SEM is 20 kV. The etching solution is a Kroll reagent (HF: HNO_3: H_2O = 5:15:80). Moreover, X-ray diffraction (XRD) was performed using Panalytical X' Pert equipment and Cu K_α radiation to confirm the phase composition. The XRD analysis was performed under an acceleration voltage of 40 kV, with a scanning range of 20–90°, a scanning speed of 6°/min, and a step size of 0.016°. The electron backscattered diffraction (EBSD) was also analyzed by Hitachi SU5000 SEM with a step size of 0.25 μm. The acceleration voltage of EBSD is 20 kV. The images were processed by AztecCrystal software. The microstructures and nano phases were further characterized by using a Talos F200X transmission electron microscope (TEM) with an acceleration voltage of 200 kV.

2.3. Mechanical properties

The tensile samples were evaluated along the build direction (Fig. 1f). The mechanical properties of plate specimens (gauge area of 15 mm × 5 mm × 1.8 mm) (Fig. 1f) were tested at room temperature with a strain rate of $8 \times 10^{-4}\ s^{-1}$ on an AGX-plus universal testing machine. The strain was measured using an electronic extensometer with a gauge of 10 mm.

3. Results

3.1. Porosity analysis and parameter optimization

To optimize the SLM printing parameters, the porosity of the as-printed TMCs was investigated using an optical microscope. As shown in Fig. S1, the pore defects of the TMC samples prepared with different SLM parameters were characterized at low magnification. Fig. 1a shows the variation trend of porosity with the increase of scanning speed laser power. With the scanning speed increasing from 400 mm/s to 1000 mm/s, the porosity of TMCs decreases with the decrease of VED. With the laser power increased from 180 to 330 W, the porosity of TMCs increases accordingly with the increase of VED. Therefore, the formation of pores in the TMCs is mainly related to inappropriate process parameters of SLM. This phenomenon arose due to the instability of the molten pool at high energy densities, which led to the formation of defects like keyholes. This conclusion was also corroborated by microstructural analysis of the TMCs, as detailed in Section 3.2. Consequently, it is suggested that a reduction in VED is conducive to decreasing the porosity of TMCs in terms of the process parameter range selected for the present study. However, the VED should not be excessively low. As shown in Fig. S2 in the Supplementary material, which illustrates the macroscopic morphology of partial as-printed TMCs, the TMCs with P = 155 W and v = 1100 mm/s (VED = 52 $J{\cdot}mm^{-3}$) exhibited significant cracking. This phenomenon can be attributed to inadequate interlayer bonding resulting from insufficient VED.

Based on preliminary research, the low laser power of 180 W was selected, and the VED was reduced by increasing the scanning speed appropriately. The pore defects in TMCs after parameter optimization are illustrated in Fig. 2c, d, e, f. Statistical analysis revealed that the porosity of the TMCs was significantly reduced to below 0.02% with parameter setting as P = 180 W and v = 1050–1200 mm/s. Fig. 2b is the 3D-CT characterization result of the sample with SLM parameters of P = 180 W and v = 1100 mm/s. The porosity is only 0.0005%, indicating that a fully dense composite is acquired by the optimization of process parameters.

3.2. Microstructure characterization

The as-printed TMCs were subjected to XRD analysis to further investigate the phase constituent, as shown in Fig. 3. It can be seen that the TMCs prepared by SLM were mainly composed of α-Ti or α′-Ti with hexagonal close-packed structures. No TiB diffraction peak was observed due to the low content and small size of TiBw. Compared to the diffraction peaks of the original alloy powder, the TMCs fabricated through SLM exhibited a shift to the right. The right shift of the diffraction peaks indicates that the spacing between the crystal planes of the as-printed TMCs decreased, which may be attributed to the residual stress existing within the interior of TMCs [28,29]. A weak β-Ti diffraction peak was observed in the region from 39° to 42°at the VED of 136 $J{\cdot}mm^{-3}$ but did not exist in the TMCs with lower VED.

To explore the influence of VED on the microstructures of the as-printed TMCs, the microstructures were examined by OM and SEM. Fig. 4a–c, e, and g show the OM images of the XOZ cross-section of the as-printed TMCs with different VEDs. On the XOZ cross-section of the TMCs, the overlapping layers of molten pools can be observed. The fish-scale morphology of the molten pools exhibits a consistent Gaussian distribution pattern, reflecting the energy profile of the laser beam [30]. The molten pools exhibited deep and narrow characteristics with the distribution of large holes at the VED of 188 $J{\cdot}mm^{-3}$ (P = 305 W, v = 600 mm/s), which is the typical keyhole pattern [31,32]. In addition, the interior of the molten pools was composed of fine prior β grains, which could be attributed to the tremendous temperature gradient at the high energy density, resulting in high undercooling and consequently refining the columnar grains. As the VED decreased, the molten pool morphology underwent a transition from a sharp to a smooth configuration, accompanied by an increase in the aspect ratio from approximately 1 to above 1.5, along with a gradual reduction in both the number and size of pores. Furthermore, the fine columnar grains in the molten pools were transformed into large columnar grains (Fig. 4a–c, e, g). The corresponding change was observed in the XOZ cross-section, where the small-sized grains within molten pools were transformed into wide equiaxed grains surrounded by narrow β grains at boundaries (Fig. S3). A similar phenomenon was observed by Eskandar et al. [20].

Fig. 4b–d, f, and h show the SEM images of the as-printed TMCs with different VEDs. The microstructures of the TMCs with VED ≥136 $J{\cdot}mm^{-3}$ (Fig. 4b–d) were composed of lamellar α+β phases. However, when the

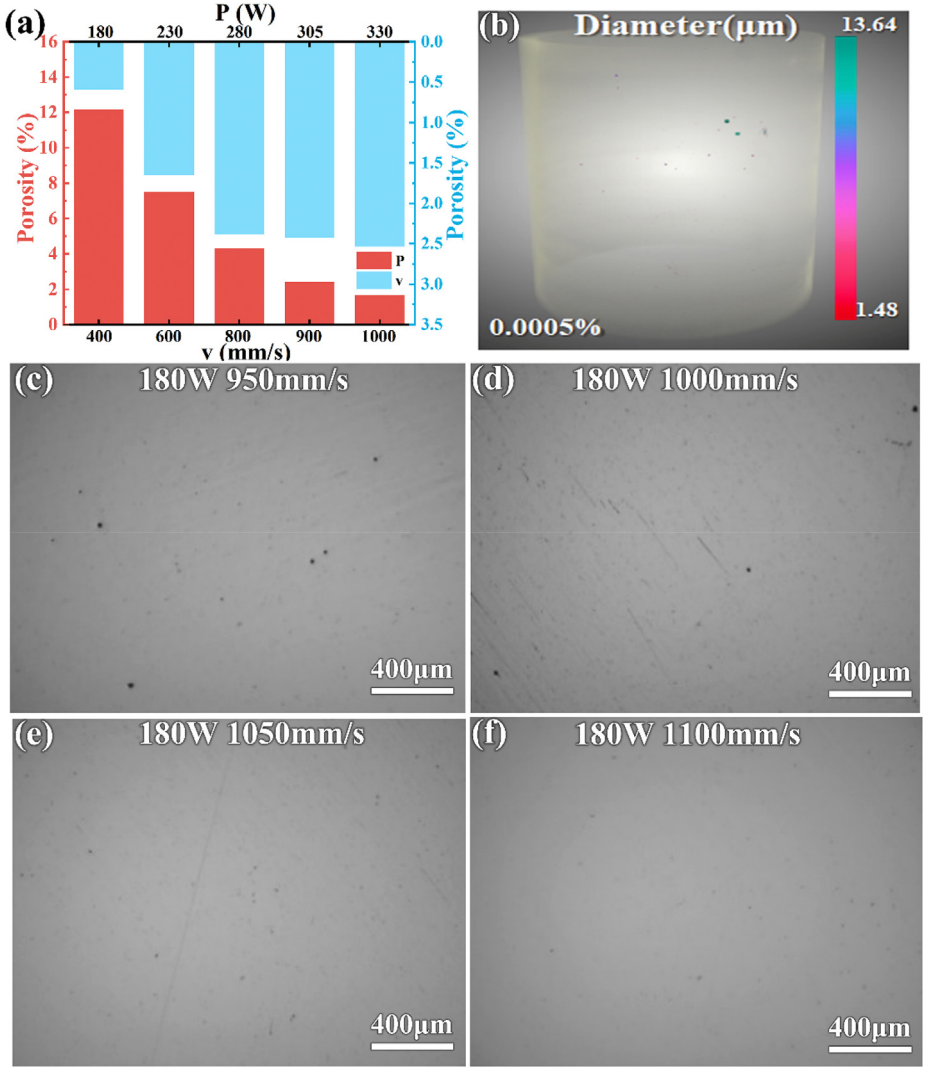

Fig. 2. Schematic representation of porosity changes and images showing the micropores in TMCs prepared by optimized parameters: (a) Illustration of the trend of porosity as the scanning speed and the laser power increased. (b) Three-dimensional CT pore detection result of TMC with SLM parameters of $P = 180$W, $v = 1100$ mm/s (c) $P = 180$W $v = 950$ mm/s, (d) $P = 180$W $v = 1000$ mm/s, (e) $P = 180$W $v = 1050$ mm/s, (f) $P = 180$W $v = 1100$ mm/s.

VED was reduced to 74 J·mm^{-3}, the size of the β phases was significantly reduced and its presence became less conspicuous (Fig. 4f). The microstructures of TMCs with the VED of 61 J·mm^{-3} (Fig. 4h) were different

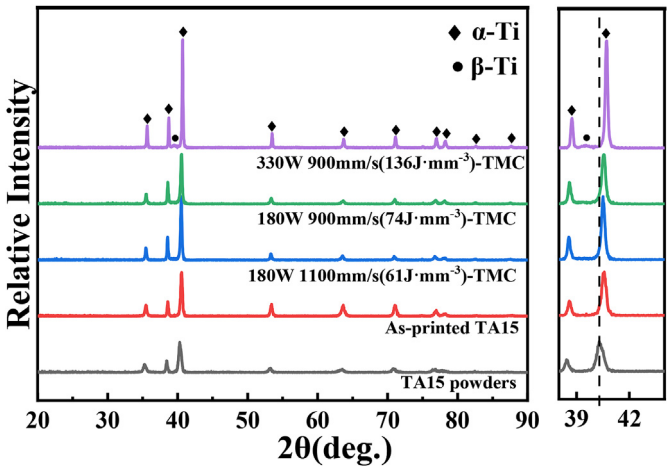

Fig. 3. XRD patterns of TMCs with different laser energy densities, as-printed alloy, and original alloy powder.

and composed of staggered hierarchical α′ martensite. Only a few nano point-like β phases precipitated in the middle and boundaries of martensite. Moreover, the distributions of TiBw in different TMCs were also different. A portion of the TiBw exhibited enrichment at the β grain boundaries, while another portion was distributed within the grains, at a high VED (≥136 J·mm^{-3}). A similar phenomenon can be observed in TMCs with the VED of 74 J·mm^{-3}. No precipitation of TiBw at grain boundaries was observed in TMCs with the VED of 61 J·mm^{-3}.

The microstructures of two cross-sections of the optimized porosity sample were further characterized based on the analysis of phase type, morphology, and energy density, as shown in Fig. 5. The XOZ and XOY cross-sections of the internal microstructures of the columnar prior β grains of TMCs are illustrated in Fig. 5a and d, respectively. The columnar prior β grains in TMCs exhibited irregular shapes and various sizes due to the scanning strategy that the scanning direction is differentiated by 67° for adjacent layers [19]. The width of the wide columnar crystal is approximately 80–90 μm, while the fine columnar crystal exhibited a width ranging from 10 μm to 20 μm. The wide columnar prior β grains were composed of hierarchical martensite. The primary martensite exhibited a parallel or vertically elongated acicular morphology with a length exceeding 10 μm. The secondary (5–10 μm), tertiary (2–5 μm), and quartic (<2 μm) martensite were arranged in parallel and vertical orientations between the primary martensite (Fig. 5b–e). The fine β

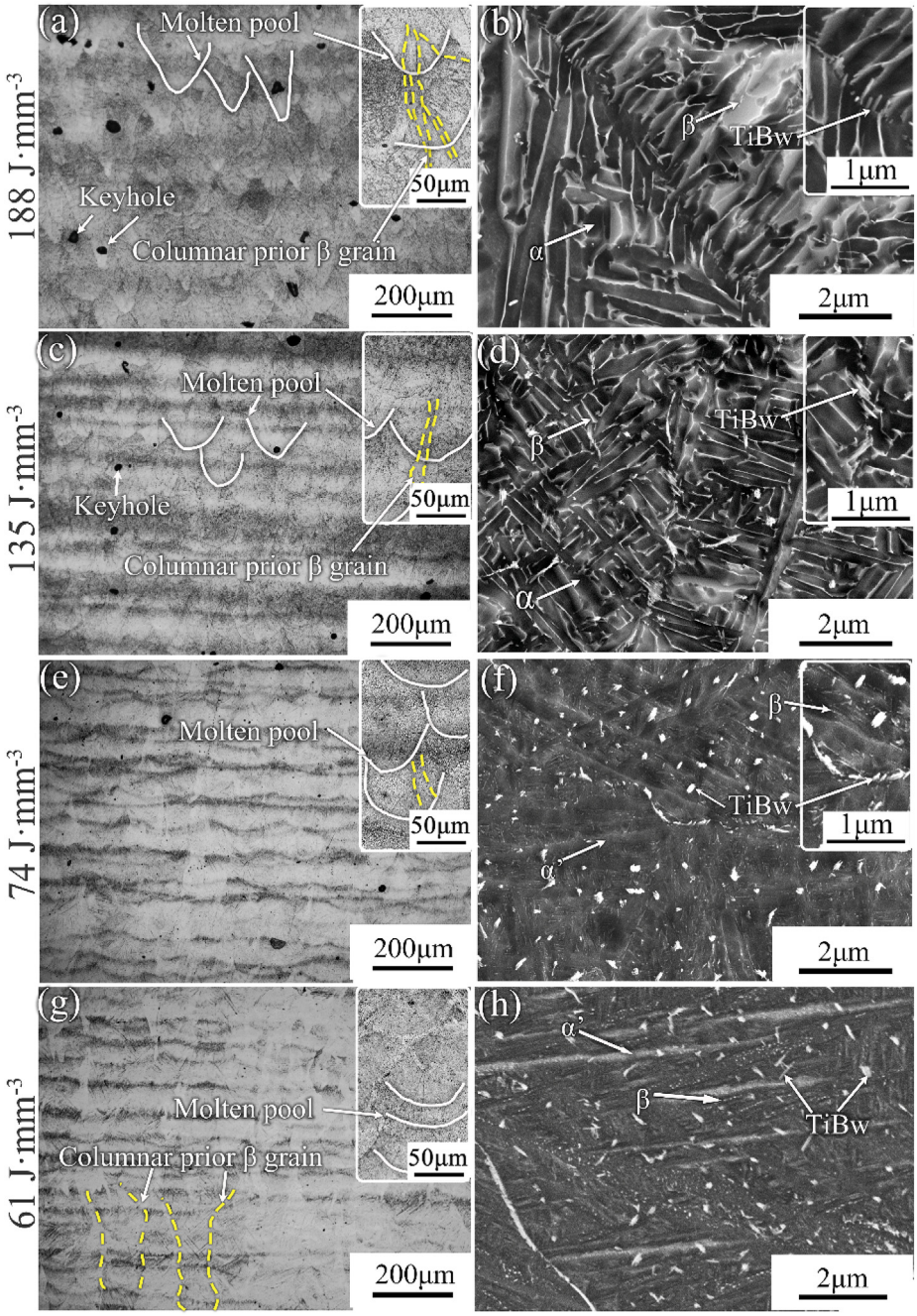

Fig. 4. OM images and SEM images of TMCs with different VEDs: (a, b) 188 J mm^{-3}, (c, d) 136 J mm^{-3}, (e, f)74 J mm^{-3}, (g, h) 61 J mm^{-3}.

grains were mainly composed of acicular martensite parallel or at a 45°–70° angle to each other, as shown in Fig. 5c and f. Yang et al. [18] proposed that during complex thermal cycling, a portion of α′ martensite transformed into the unstable β phase, which can subsequently either transform into quartic martensite or remain within the matrix directly.

The nano scale β phase and TiBw were further characterized with TEM. Fig. 6 shows the TEM images of the as-printed TMCs (61 J·mm^{-3}). The white box in Fig. 6a was selected for EDS analysis (Fig. 6b). EDS results revealed the segregation of the Mo element at the martensite boundary, which was the stable element of β phase. Consequently, it can be deduced that a limited quantity of β phase precipitated at the martensite boundary. The EDS analysis also revealed the presence of an accumulation area of B element within this region, which was presumed to be a TiBw here according to Ref. [33]. Fig. 6c shows the diffraction pattern of the substrate, which corresponds to the α'/α-Ti phase with the HCP structure. After calibrating the pattern obtained by Fourier transform (Fig. 6d), it is confirmed that the whisker was the TiBw with a B27 structure [25]. Moreover, it can be seen from the FFT image that the TiBw exhibited a significant abundance of stacking faults.

EBSD was employed to conduct a detailed investigation of the martensite structure in TMCs and to analyze the orientation relationship between the phases. The XOZ cross-section of the TMCs composite (61 J·mm^{-3}) was ground and electrolytically polished for EBSD characterization (Fig. 7). The needle-like martensite can be observed in Fig. 7a presenting a net-basket arrangement. From the pole map in Fig. 7b, it is concluded that the {0001} direction and $\{11\bar{2}0\}$ direction of the material exhibited weak texture along the construction direction. The orientation relationships between α′-Ti and original β-Ti can be expressed as $\{0001\}_{\alpha'}//\{110\}_{\beta}$, $\{11\bar{2}0\}_{\alpha'}//\{111\}_{\beta}$ [34]. When body-centered cubic β-Ti was transformed into hexagonal close-packed α/α′-Ti, the

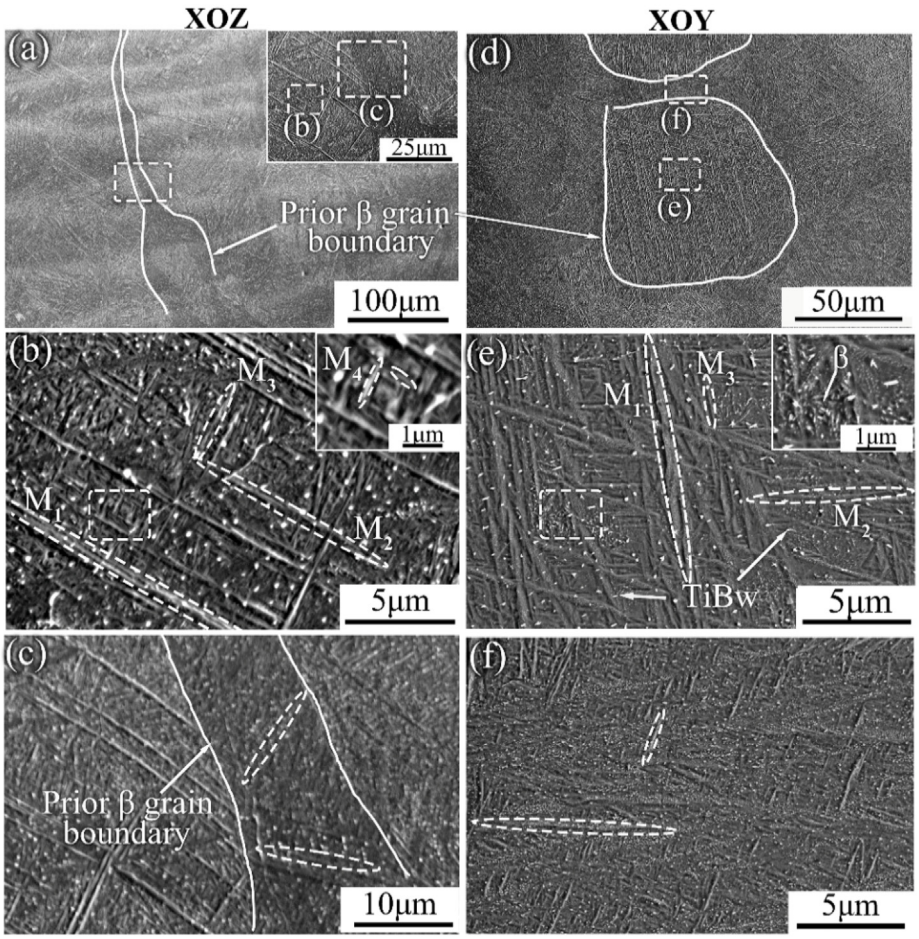

Fig. 5. SEM images of the as-printed TMC (61 J mm^{-3}) at XOZ cross-section: (a) macroscopic morphology at low magnification, (b) internal microstructures of large columnar grains, (c) internal microstructures of fine columnar grain between large columnar grains. SEM of the as-printed TMC (61 J mm^{-3}) at XOY cross-section: (d) macroscopic morphology at low magnification, (e) internal microstructure of equiaxed grains, (f) microstructure of fine β grains between equiaxed grains.

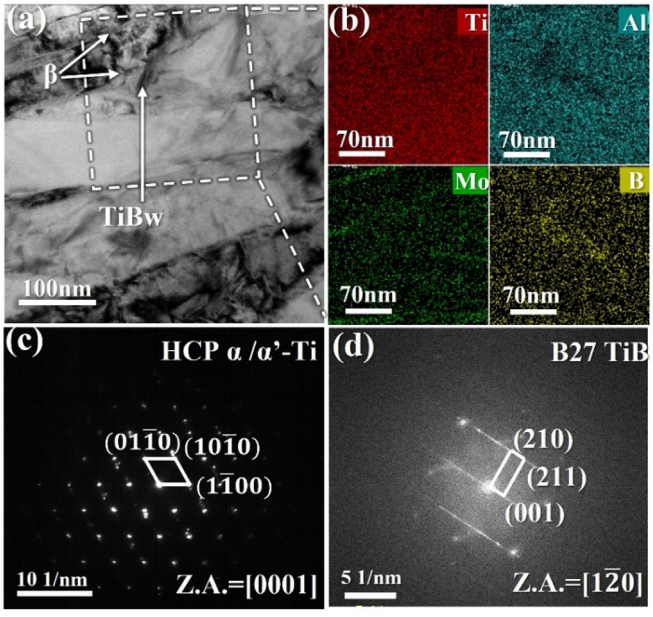

Fig. 6. TEM of the as-printed TMC (61 J·mm^{-3}): (a) bright field image, (b) EDS, (c) diffraction spot of the matrix, (d) FFT of the whisker.

close-packed plane $\{110\}_{\beta}$ was parallel to the close-packed plane $\{0001\}_{\alpha/\alpha'}$, and the close-packed direction $<111>_{\beta}$ was parallel to the close-packed direction $<11\bar{2}0>_{\alpha/\alpha'}$, which met Burgers orientation relationship [35]. According to the Burgers orientation relationship, the parent phases were reconstructed according to the obtained EBSD results (Fig. 7c). It can be observed that the obvious large columnar grains were along the building direction. In addition, the α′ martensite thickness of TMCs and alloy was statistically analyzed to investigate the effect of nano TiBw. The α′ martensite thickness of as-printed alloy and TMC are 1.5 ± 0.5 μm and 0.9 ± 0.3 μm in Fig. 7d, e, f, and g, respectively, which can be attributed to TiBw serving as nucleation positions for α′-Ti [36] and inhibiting the growth of α′-Ti [21]. The refinement of martensite is conducive to the enhancement of strength.

3.3. Tensile properties

The mechanical properties of the as-printed TMCs were evaluated both before and after parameter optimization. Fig. S4 illustrates the tensile curves and statistical diagram of the mechanical properties and porosity changes in the printed TMCs without parameter optimization. It is evident that strength increases as porosity decreases. Consequently, optimizing SLM parameters that minimize pore defects is the critical factor in achieving higher strength.

The as-printed TMCs with low porosity (<0.02%) were selected for tensile test at room temperature, while the as-printed alloy was also tested for comparison. Fig. 8a presents the tensile curves for the TMCs

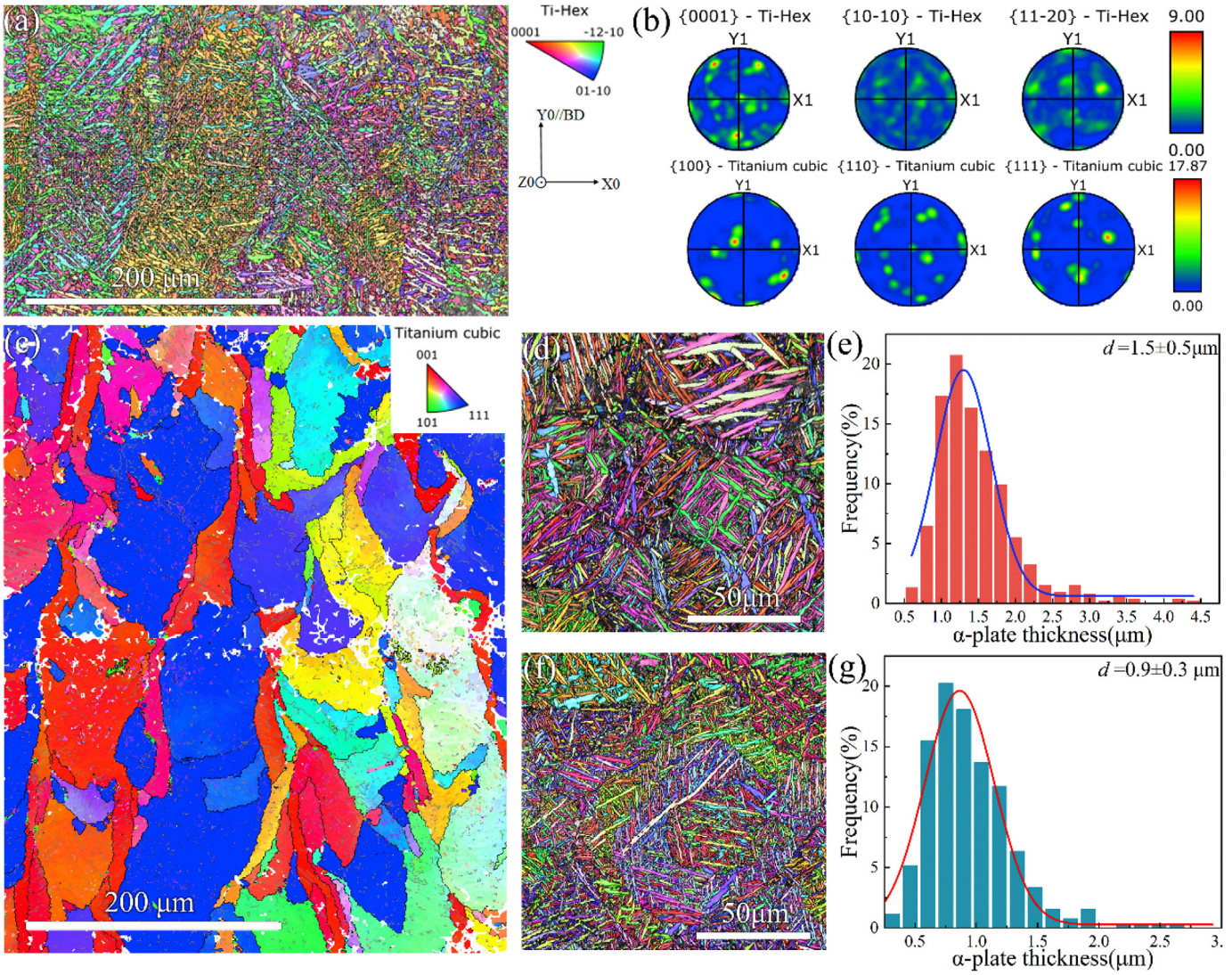

Fig. 7. EBSD analysis for the as-printed TMC (61 J·mm^{-3}): (a) IPF + BC, (b) pole map, (c) reconstructed IPF map of primary β, (d) IPF + BC map and (e) α′ martensite plate thickness statistical map of the as-printed alloy, (f) IPF + BC map and (g) α′ martensite plate thickness statistical map of the as-printed TMCs.

and the corresponding results are summarized in Table 1. Fig. 8b illustrates a columnar statistical representation of the associated tensile strength, yield strength, and elongation. When the laser power was 180 W and the scanning speed increased from 1050 mm/s to 1200 mm/s, the strength, and plasticity of TMCs exhibited an increase trend from 63 J·mm^{-3} to 56 J·mm^{-3} and then decreased. The TMCs with SLM parameters of P = 180 W and v = 1100 mm/s (VED = 61 J·mm^{-3}) with a limited number of pore defects exhibited the highest strength and plasticity and minor discrepancies indicating stable performance. The highest tensile strength and yield strength of TMCs are 1432 MPa and 1320 MPa, respectively, which are 17% (206 MPa) and 24% (252 MPa) higher than those of the as-printed alloy (σ_b = 1226 MPa, σ_s = 1068 MPa). The finer martensite in the TMCs contributed to the strength improvement. The presence of finer martensite also led to a slight reduction in ductility, measured to be 4.0% lower than the value of 6.3% of the alloy. Compared with the properties of as-printed TMCs reported, the TiBw/Ti6.5Al2.5Zr1Mo1V composite in this work shows a better strength-ductility synergy (Fig. 8c). The incorporation of minor TiB induced the detrimental impact of the brittle phase on the plasticity, thereby maintaining a relatively high level of elongation in the as-printed TMCs. Furthermore, owing to the presence of TiB and the substantial reduction in defects through the optimization of SLM parameters, the strength remains at a considerably high level. Therefore, the VED of 61 J·mm^{-3} was considered to be close to the optimal laser energy density.

Fig. S5 illustrates the tensile fractures of the as-printed TMCs and Ti6.5Al2.5Zr1Mo1V alloy. The fracture surface of the as-printed TMCs (Figs. S5a, b, c) revealed numerous cleavage surfaces and steps with a significant presence of dimples distributed on the cleavage surfaces, indicating micro-pore aggregation fractures and quasi-cleavage fractures in certain regions. As illustrated in Figs. S5d, e, and f, the fracture surface of the Ti6.5Al2.5Zr1Mo1V alloy exhibited a rough texture characterized by extensive dimples, with micropore aggregation identified as the primary fracture mechanism. It was observed that the dimple size and depth of the as-printed TMCs were significantly smaller than those of the as-printed alloy, indicating that the ductility of the TMCs is relatively inferior, consistent with the results obtained from the tensile test.

4. Discussion

4.1. Microstructure evolution during SLM

When each layer of powder melts and solidifies, the solidified former layer would be subsequently reheated and remelted. The reason for columnar grain formation is that the prior β grains always grow parallel to the maximum thermal gradient direction during SLM [41]. The direction of heat flow within the molten pools is from the top to the bottom,

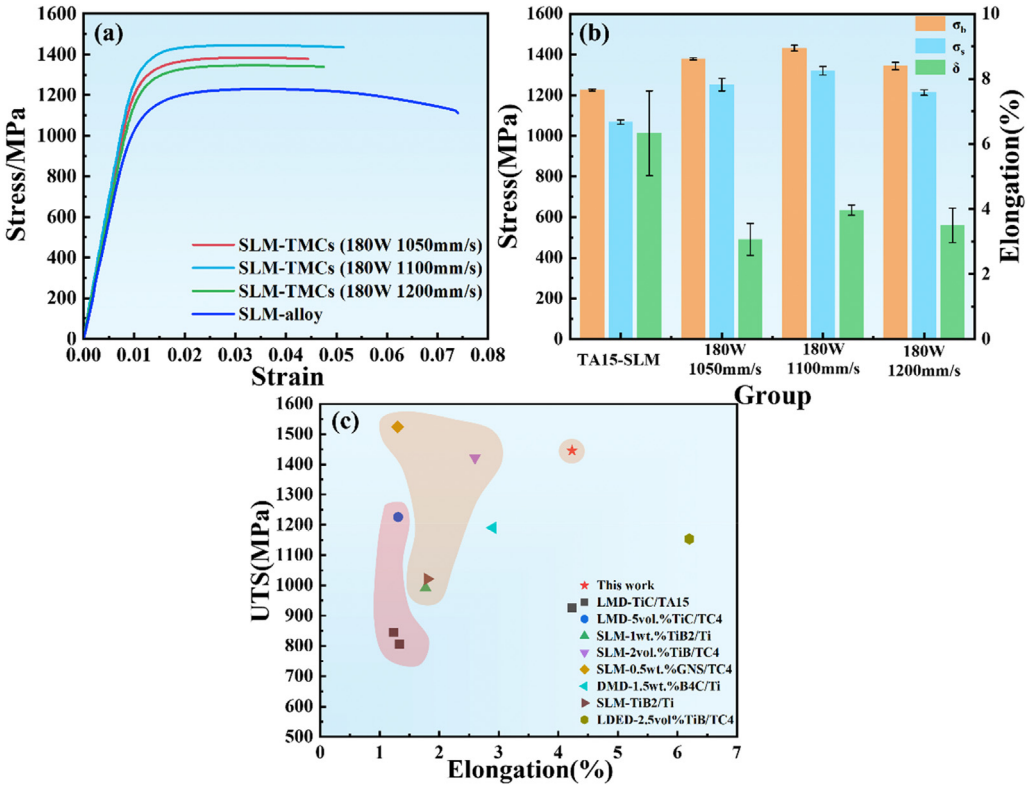

Fig. 8. The tensile mechanical properties: (a) Tensile curves of the as-printed alloy and TMCs at room temperature. (b) Statistical diagram of mechanical properties of the as-printed alloy and TMCs at room temperature. (c) The tensile strength of TMCs prepared by different processing routes with various reinforcement contents [5, 21,22,27,37–40].

while the grains grow along the construction direction, opposing the heat flow. Due to the layer-by-layer manufacturing characteristic of SLM, grains grow continuously through multiple molten pools, ultimately forming columnar grains [42]. Furthermore, the laser scanning pathway rotates 67° per layer during SLM resulting in the irregular shapes of the columnar prior β grains. Temperature gradient G (°C/min) and solidification rate R (m/s) determine the morphology and size of prior β grains [43]. The G/R ratio indicates constitutional undercooling, influencing grain characteristics. If G/R exceeds a critical threshold, prior β grains grow in a columnar pattern. $G{\cdot}R$ represents the cooling rate and determines the size of prior β grains. A high cooling rate limits the growth and promotes the refinement of prior β grains, further promoting the refinement of martensitic structure.

The interior of the prior β grains is mainly composed of a hierarchical structure of martensite. The classification phenomenon of martensite was mainly related to the complex thermal cycles in the SLM process [18]. The researchers attributed the thermal cycles undergone by the Nth layer material to five distinct intervals.

(i) In the first thermal cycle, the temperature is sufficiently elevated to induce the melting of martensite, which subsequently undergoes solidification to generate primary martensite.
(ii) In the second thermal cycle, the temperature of the *N*th layer rises to a range between the solid and liquid phase, leading to the following phase transition: α' →β+L→α'.
(iii) In the third thermal cycle, the temperature of the *N*th layer could only transform α′ into β phase, while some dislocations are retained inside the β phase to form primary and secondary martensite.
(iv) In the fourth thermal cycle, the temperature of the *N*th layer is between the martensite and the β transition temperature. The previously generated martensite undergoes a transformation into the β phase, while the β phase is further transformed into the small size and unstable α′ phase.
(v) In the fifth thermal cycle, the temperature is below the martensite transition temperature, so the previously formed primary, secondary, and tertiary martensite experience slight coarsening.

Table 1
The mechanical properties of the as-printed alloy and TMCs at room temperature.

Group	VED (J·mm^{-3})	σ_b (MPa)	σ_y (MPa)	δ(%)
Ti6.5Al2.5Zr1Mo1V alloy	–	1226 ± 5	1068 ± 11	6.3 ± 1.3
TMCs	63(180W 1050 mm/s)	1379 ± 5	1252 ± 30	3.1 ± 0.5
	61(180W 1100 mm/s)	1432 ± 14	1320 ± 13	4.0 ± 0.2
	56(180W 1200 mm/s)	1344 ± 18	1213 ± 13	3.5 ± 0.5

During multiple thermal cycles, a part of α′ martensite decomposes into α+β or β phases, with these β phases either retained in the material or transformed into smaller-sized α′ martensite, which is the quaternary martensite under the action of dislocations or twins. However, with higher laser energy input, the heat-affected zone of the TMCs expands and the already solidified part undergoes more thermal cycles. When multiple thermal cycles occur below the martensite transition temperature, it can be thought of as a low-temperature heat treatment of TMCs, resulting in a decomposition of martensite into α+β phase, as shown in Fig. 4b and d. This further elucidates the observation of the β phase diffraction peak at the high VED (136J·mm^{-3}).

According to the above discussion, the microstructural evolution mechanism of a single molten pool during the SLM process is summarized in Fig. 9. The laser beam irradiates the powder, inducing powder melting

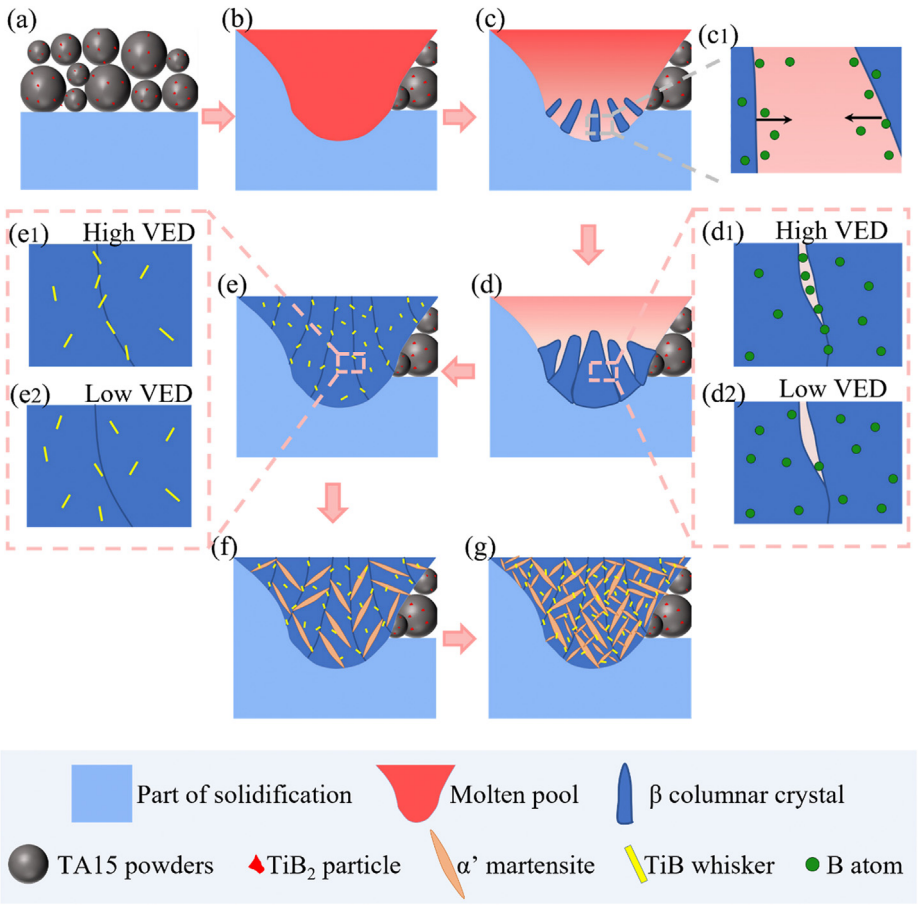

Fig. 9. The microstructure evolution mechanism of a single molten pool during SLM.

and resulting in the formation of a molten pool (Fig. 9a and b). As the temperature decreases during solidification, the temperature at the bottom of the melt pool initially reaches the β transition temperature, followed by the growth of prior β columnar grains along the direction of the temperature gradient (Fig. 9c and d). Due to the Marangoni convection [34] in the molten pool and the diffusion effect of B atoms, B atoms are distributed throughout the molten pools. When the liquid phase and the β phase coexist, the B atom tends to be expelled by the β phase and enriches at the solid-liquid interface due to its limited solubility in the β phase (Fig. 9c1). During the cooling and solidification process, B atoms react with the Ti matrix to precipitate TiBw. However, the solubility limit of B atoms in the β phase is increased because of the extremely fast cooling rate of SLM technology (10^4–10^6 K·s^{-1}) [44]. Therefore, a part of the B atoms dissolves in the β phase, leading to the precipitation of TiBw distributed within the columnar grains. A higher energy density always leads to a lower cooling rate which leads to enhancing the rejection of β phase towards B atoms (Fig. 9d1). Conversely, at low energy densities, the concentration of B atoms at grain boundaries is less pronounced attributed to the diminished rejection of β phase towards B atoms resulting from the higher cooling rate (Fig. 9d2). Consequently, the distribution of TiBw varies with changes in VED (Fig. 9e1, e2), consistent with the observations presented in Fig. 6. As the temperature further decreases, martensitic transformation is induced (Fig. 9f). After several thermal cycles, the hierarchical martensitic structure is established with a diffuse distribution of nano TiBw (Fig. 9g).

4.2. Strengthening mechanism

The tensile test results show that the strength of the as-printed TMCs alloy is significantly improved compared with that of alloy. The strengthening mechanism of the TMCs was analyzed.

Due to the extremely fast cooling rate of SLM, the TMCs prepared by SLM have finer grains than the material prepared by conventional methods. According to Fig. 8, the martensite thickness of the TMCs is finer than that of the alloy prepared by SLM due to the existence of TiB. Grain refinement increases the volume fraction of grain boundaries, which hinders the dislocation movement and thus improves the material's strength [45]. The strengthening effect of grain refinement on the strength of the composite can be estimated by the Hall-Petch formula [46]:

$$\sigma_{HP} = k_y\left(d_1^{-0.5} - d_2^{-0.5}\right), \tag{3}$$

where k_y is the strengthening coefficient (0.91 MPa·m$^{0.5}$ in DRTMCs) [46], d_1 is the average thickness of acicular martensite in TMCs (m), d_2 is the average thickness of acicular martensite in alloy (m).

According to Eq. (4), the contribution of grain refinement strengthening to the yield strength of the TMCs is calculated to be about 216 MPa.

The TiBw plays a role in load transfer strengthening. According to the statistics of Image J of Fig. 4h, the average aspect ratio of TiBw is about 8.23. The load transfer effect can be estimated using a modified shear-lag model [38]:

$$\Delta\sigma_{LT} = \frac{1}{2}V_{TiB}\sigma_{ym}\frac{l_{TiB}}{d_{TiB}}\omega_0, \tag{4}$$

where V_{TiB} is the volume fraction of TiBw in the composite (0.85 vol%), σ_{ym} is the yield strength of the as-printed alloy, $\frac{l_{TiB}}{d_{TiB}}$ is the aspect ratio of TiBw (l_{TiB} and d_{TiB} are the average length and the average diameter of TiBw, respectively), ω_0 is orientation factor of TiBw.

According to Eq. (4), the contribution of whisker load transfer

strengthening to the yield strength of the TMC is about 4.7 MPa.

When the size of the reinforcements is smaller than 1 μm, the reinforcements block the movement of dislocations on the matrix slip surface in the way of dislocation loops during deformation. The corresponding contribution of Orowan looping strengthening to the improvement of material yield strength reads [47].

$$\Delta\sigma_{oro} = \frac{0.13 G_m b}{\lambda} \ln \frac{D_{TiB}}{2b}, \tag{5}$$

where G_m is the shear modulus of the alloy, b is the Burgers vector of the α-Ti matrix, D_{TiB} is the equivalent diameter of TiBw, and λ is the interparticle spacing.

G_m could be expressed as [38].

$$G_m = \frac{E}{2(1+\nu)}, \tag{6}$$

where E is the elastic modulus of the as-printed alloy, and ν (=0.39) is Poisson's ratio of alloy.

D_{TiB} could be expressed as [45].

$$D_{TiB} = \sqrt[3]{1.5 d_{TiB}^2 l_{TiB}}, \tag{7}$$

λ could be expressed as [48].

$$\lambda \approx D_{TiB}\left[(2V_{TiB})^{-\frac{1}{3}} - 1\right]. \tag{8}$$

According to Eqs. (6)–(9), the contribution of Orowan looping strengthening to the yield strength of the TMC is about 33.4 MPa.

Due to the low solubility of B atoms in the Ti matrix, the solid solution strengthening effect can be neglected. In addition, the thermal expansion coefficients of TiBw and alloy are close. Thus, the stress caused by thermal mismatch strengthening can also be neglected.

Therefrom, the theoretical yield strength of TMC prepared by SLM can be calculated by [51].

$$\sigma_y = \sigma_{ym} + \Delta\sigma_{HP} + \Delta\sigma_{LT} + \Delta\sigma_{oro}. \tag{9}$$

Using Eqs. (4)–(10) and the data presented in Table 2, the theoretical yield strength of the as-printed TMCs composite is calculated to be 1322.1 MPa, which is consistent with the experimental data (1320 ± 13 MPa). Table 3 summarizes the contribution values of several strengthening mechanisms for yield strength improvement.

The effect of grain refinement strengthening is the most significant, accounting for about 85.0% of the total strengthening strength. The Orowan looping strengthening caused by nanoscale TiBw accounted for 13.1%. The strengthening effect of load transfer is only 1.9% due to the small amount of TiBw added. In general, the grain refinement caused by the addition of TiBw, the hindrance effect of nano TiBw on dislocation, and the load transfer effect of TiBw itself effectively improve the strength of as-printed TMC.

Table 2
Properties and parameters in the calculation.

Properties and parameters	Value	Source
k_y (MPa·m$^{0.5}$)	0.91	[46]
d_1 (μm)	0.9 ± 0.3	Measured and calculated
d_2 (μm)	1.5 ± 0.5	Measured and calculated
ω_0	0.125	[49]
l_{TiB} (nm)	298.71	Measured
d_{TiB} (nm)	36.28	Measured
l_{TiB}/d_{TiB}	8.23	Measured and calculated
E (GPa)	118.33 ± 3.21	Measured and calculated
b (nm)	0.295	[50]
D_{TiB} (nm)	83.86	Calculated

Table 3
Properties and parameters in the calculation.

Strengthening mechanism	Value (MPa)	Proportion in the total Δσ (%)
$\Delta\sigma_{HP}$	216.2	85.0
$\Delta\sigma_{LT}$	4.7	1.9
$\Delta\sigma_{oro}$	33.4	13.1

5. Conclusions

In this study, 0.85 vol%TiBw/Ti6.5Al2.5Zr1Mo1V composites with almost fully dense microstructure have been prepared by SLM. The influence of nano TiBw on microstructure evolution and mechanical properties is systematically explored. The main conclusions are as follows.

(1) As the VED decreases from 282 J·mm^{-3} to 56 J·mm^{-3}, the energy conduction mode of the molten pool undergoes a transition from the keyhole mode to the conduction mode, resulting in a decrease in the porosity of the TMCs. When the VED varies between 56 and 64 J·mm^{-3}, the porosity of the as-printed TMCs has diminished to below 0.02%. The optimized VED is around 61 J·mm^{-3} (P = 180 W, v = 1100 mm/s), where the porosity is only 0.0005 %, achieving a fully dense state.

(2) The as-printed TMCs exhibit significant irregularities in the form of large columnar prior β grains along the building direction. Within these prior β grains, a hierarchical α′ martensitic structure is observed. The nano TiBw is dispersed throughout the matrix. As the VED increases, the matrix microstructures transform martensite to lamellar α+β, accompanied by the precipitation and aggregation of TiBw at the prior β grain boundaries. During thermal cycling, the nano TiBw is found to inhibit the coarsening of the martensite.

(3) The TMCs with the SLM parameter of P = 180 W and v = 1100 mm/s (VED = 61 J·mm^{-3}) achieve a synergistic increase in strength and elongation by adding minor TiBw. Specifically, the tensile strength, yield strength, and elongation of the as-printed TMCs are 1446 MPa, 1338 MPa, and 4.0%, respectively. The enhancement in yield strength of these TMCs can be attributed to grain refinement strengthening, load transfer strengthening, and Orowan strengthening.

CRediT authorship contribution statement

Qi An: Writing – review & editing, Writing – original draft, Funding acquisition. **Lihua Cui:** Writing – review & editing, Writing – original draft, Formal analysis. **Delong Gong:** Writing – review & editing, Formal analysis. **Han Cheng:** Formal analysis. **Ying Liu:** Formal analysis. **Rui Zhang:** Writing – review & editing. **Yang Bao:** Writing – review & editing. **Lujun Huang:** Writing – review & editing, Funding acquisition. **Lin Geng:** Writing – review & editing.

Declaration of competing interest

The authors declare that they have no known competing financial interests or personal relationships that could have appeared to influence the work reported in this paper.

Acknowledgements

This work was financially supported by the National Natural Science Foundation of China (Grant Nos. 52371135, 52201156, 52261135543, and 52401039), China Postdoctoral Science Foundation (Grant No. 2024T171151), the Young Elite Scientists Sponsorship Program by CAST (Grant No. 2023QNRC001), and the Heilongjiang Touyan Team

Program.

Appendix A. Supplementary data

Supplementary data to this article can be found online at https://doi.org/10.1016/j.tramat.2025.100014.

References

[1] J.A. Otte, J. Zou, M.S. Dargusch, High strength and ductility of titanium matrix composites by nanoscale design in selective laser melting, J. Mater. Sci. Technol. 118 (2022) 114–127, https://doi.org/10.1016/j.jmst.2021.12.020.

[2] M.J. Xia, A.H. Liu, Z.W. Hou, N.L. Li, Z. Chen, H.Y. Ding, Microstructure growth behavior and its evolution mechanism during laser additive manufacture of *in situ* reinforced (TiB+TiC)/Ti composite, J. Mater. Sci. Technol. 728 (2017) 436–444, https://doi.org/10.1016/j.jallcom.2017.09.033.

[3] N. Kang, P. Coddet, Q. Liu, H. Liao, C. Coddet, *In situ* TiB/near α Ti matrix composites manufactured by selective laser melting, 3D Print, Addit. Manuf. 11 (2016) 1–6, https://doi.org/10.1016/j.addma.2016.04.001.

[4] Z.G. Zhou, Y.Z. Liu, X.H. Liu, Constructing targeted bi-lamellar microstructure via heat treatment for high compressive strength and plasticity in selective laser melted Ti6Al4V-5vol%TiB composite, Mater. Sci. Eng., A 844 (2022) 143173, https://doi.org/10.1016/j.msea.2022.143173.

[5] H.L. Li, Z.H. Yang, D.L. Cai, D.C. Jia, Y. Zhou, Microstructure evolution and mechanical properties of selective laser melted bulk-form titanium matrix nanocomposites with minor B4C additions, Mater. Des. 185 (2020), https://doi.org/10.1016/j.matdes.2019.108245.

[6] G. Shun, Y.N. Li, J.R. Gu, J. Liu, Y. Peng, P.K. Wang, Q. Zhou, K.H. Wang, Microstructure and mechanical properties of Ti6Al4V/B_4C titanium matrix composite fabricated by selective laser melting (SLM), J. Mater. Res. Technol. 23 (2023) 1934–1946, https://doi.org/10.1016/j.jmrt.2023.01.126.

[7] Q. Wang, B. Jin, Quan, L.Z. Zhao, X.L. Liu, A.J. Pan, X.F. Ding, W. Gao, Y.F. Song, X.F. Zhang, Microstructural evolution and mechanical behavior of TA15 titanium alloy fabricated by selective laser melting: influence of solution treatment and aging, Metals 13 (2023) 1514, https://doi.org/10.3390/met13091514.

[8] H. Chen, G.B. Mi, P.J. Li, C.X. Cao, Excellent high-temperature strength and ductility of graphene oxide reinforced high-temperature titanium alloy matrix composite fabricated by hot isostatic pressing and heat treatment, Compos. Commun. 30 (2022) 101077, https://doi.org/10.1016/j.coco.2022.101077.

[9] H. Attar, K.G. Prashanth, L.C. Zhang, M. Calin, L.V. Okulov, S. Scudino, C. Yang, J. Eckert, Effect of powder particle shape on the properties of in situ Ti-TiB composite materials produced by selective laser melting, J. Mater. Sci. Technol. 1001 (2015), https://doi.org/10.1016/j.jmst.2015.08.007.

[10] Z.G. Zhou, Y.Z. Liu, New insights into the evolution of TiB whisker and TiC particle during selective laser melting of titanium matrix composites, Mater. Sci. Eng., A 877 (2023) 145200, https://doi.org/10.1016/j.msea.2023.145200.

[11] T. Chen, W.S. Cai, Z. Liu, H.W. Ma, S.G. Qu, W.W. Zhang, C. Yang, *In situ* dual-deoxidation design of advanced titanium matrix composites by pressureless sintering, Composites, Part B 244 (2022), https://doi.org/10.1016/j.compositesb.2022.110202.

[12] P. Huo, Z. Zhao, W. Du, Z. Zhang, P. Bai, D. Tie, Deformation strengthening mechanism of in situ TiC/TC4 alloy nanocomposites produced by selective laser melting, Composites, Part B 225 (2021), https://doi.org/10.1016/j.compositesb.2021.109305.

[13] S.C. Tjong, Z.Y. Ma, Microstructural and mechanical characteristics of in situ metal matrix composites, Mater. Sci. Eng. R 29 (2000) 49–113.

[14] M.D. Hayat, H. Singh, Z. He, P. Cao, Titanium metal matrix composites: an overview, Composites, Part A 121 (2019) 418–438, https://doi.org/10.1016/j.compositesa.2019.04.005.

[15] J.L. Zhang, B. Song, C. Cai, L.J. Zhang, Y.S. Shi, Tailorable microstructure and mechanical properties of selective laser melted TiB/Ti6Al4V composite by heat treatment, Adv. Powder Mater. 1 (2022), https://doi.org/10.1016/j.apmate.2021.10.001.

[16] G.W. Qiao, B. Zhang, Q. Bai, Y. Gao, Ming, W. Du, Y.W. Zhang, Machinability of TiC-reinforced titanium matrix composites fabricated by additive manufacturing, J. Manuf. Process. 76 (2022) 412–418, https://doi.org/10.1016/j.jmapro.2022.02.033.

[17] P. Wang, J. Eckert, K.G. Prashanth, M.W. Wu, I. Kaban, L.X. Xi, S. Scudino, A review of particulate-reinforced aluminum matrix composites fabricated by selective laser melting, Trans. Nonferrous Metals Soc. China 30 (2020) 2001–2034, https://doi.org/10.1016/S1003-6326(20)65357-2.

[18] J. Yang, H. Yu, J. Yin, M. Gao, Z. Wang, X. Zeng, Formation and control of martensite in Ti-6Al-4V alloy produced by selective laser melting, Mater. Des. 108 (2016) 308–318, https://doi.org/10.1016/j.matdes.2016.06.117.

[19] Q.H. Jiang, S. Li, S. Guo, M.W. Fu, B. Zhang, Comparative study on process-structure-property relationships of TiC/Ti6Al4V and Ti6Al4V by selective laser melting, Int. J. Mech. Sci. 241 (2023), https://doi.org/10.1016/j.ijmecsci.2022.107963.

[20] F. Eskandar, G. Ali, E. Mohamed, Unique opportunities for microstructure engineering via trace B4C addition to Ti-6Al-4V through laser powder bed fusion process: as-built and heat-treated scenarios, Addit. Manuf. 50 (2022), https://doi.org/10.1016/j.addma.2021.102557.

[21] Z.G. Zhou, Y.Z. Liu, X.H. Liu, Q.K. Zhan, K.D. Wang, Microstructure evolution and mechanical properties of *in situ* Ti6Al4V-TiB composites manufactured by selective laser melting, Composites, Part B 207 (2021) 108567, https://doi.org/10.1016/j.compositesb.2020.108567.

[22] J.D. Wang, L.Q. Li, C.W. Tan, H. Liu, P.P. Lin, Microstructure and tensile properties of TiCp/Ti6Al4V titanium matrix composites manufactured by laser melting deposition, J. Mater. Process. Technol. 252 (2018) 524–536, https://doi.org/10.1016/j.jmatprotec.2017.10.005.

[23] M.S. Xie, S. Huang, Z. Wang, U. Ramamurty, High-temperature fracture behavior of an α/β Titanium alloy manufactured using laser powder bed fusion, Acta Mater. 277 (2024) 120211, https://doi.org/10.1016/j.actamat.2024.120211.

[24] M. Laleh, E. Sadeghi, R.I. Revilla, Q. Chao, N. Haghdadi, A.E. Hughes, W. Xu, I. De Graeve, M. Qian, I. Gibson, M.Y. Tan, Heat treatment for metal additive manufacturing, Prog. Mater. Sci. 133 (2023), https://doi.org/10.1016/j.pmatsci.2022.101051.

[25] H. Attar, M. Bönisch, M. Calin, L.-C. Zhang, S. Scudino, J. Eckert, Selective laser melting of in situ titanium-titanium boride composites: processing, microstructure and mechanical properties, Acta Mater. 76 (2014) 13–22, https://doi.org/10.1016/j.actamat.2014.05.022.

[26] S.L. Li, S.F. Li, L. Liu, H.Y. Liu, C.Y. Wang, P.J. Withers, Y.T. Zhu, L.N. Gao, S.D. Wang, B. Chen, W. Huo, Tu, J.B. Gao, X. Zhang, B. Li, High-temperature "Inverse" Hall-Petch relationship and fracture behavior of TA15 alloy, Int. J. Plast. 176 (2024) 103951, https://doi.org/10.1016/j.ijplas.2024.103951.

[27] M.K. Tang, L.C. Zhang, N. Zhang, Microstructural evolution, mechanical and tribological properties of TiC/Ti6Al4V composites with unique microstructure prepared by SLM, Mater. Sci. Eng., A 814 (2021), https://doi.org/10.1016/j.msea.2021.141187.

[28] B. Yang, Z. Shang, J. Ding, J. Lopez, W. Jarosinski, T. Sun, N. Richter, Y. Zhang, H. Wang, X. Zhang, Investigation of strengthening mechanisms in an additively manufactured Haynes 230 alloy, Acta Mater. 222 (2022), https://doi.org/10.1016/j.actamat.2021.117404.

[29] J. Fu, H. Li, X. Song, M.W. Fu, Multi-scale defects in powder-based additively manufactured metals and alloys, J. Mater. Sci. Technol. 122 (2022) 165–199, https://doi.org/10.1016/j.jmst.2022.02.015.

[30] C.L. Tan, K.S. Zhou, W.Y. Ma, P.P. Zhang, M. Liu, T.C. Kuang, Microstructural evolution, nanoprecipitation behavior and mechanical properties of selective laser melted high-performance grade 300 maraging steel, Mater. Des. 134 (2017) 23–34, https://doi.org/10.1016/j.matdes.2017.08.026.

[31] C. Zhao, B. Shi, S.L. Chen, D. Du, T. Sun, B.J. Simonds, K. Fezzaa, A.D. Rollett, Laser melting modes in metal powder bed fusion additive manufacturing, Rev. Mod. Phys. 94 (2022) 045002, https://doi.org/10.1103/RevModPhys94.045002.

[32] W.E. King, H.D. Barth, V.M. Castillo, G.F. Gallegos, J.W. Gibbs, D.E. Hahn, C. Kamath, A.M. Rubenchik, Observation of keyhole-mode laser melting in laser powder-bed fusion additive manufacturing, J. Mater. Process. Technol. 214 (2014) 2915–2925, https://doi.org/10.1016/j.jmatprotec.2014.06.005.

[33] L. Thijs, F. Verhaeghe, T. Craeghs, J.V. Humbeeck, J.P. Kruth, A study of the microstructural evolution during selective laser melting of Ti–6Al–4V, Acta Mater. 58 (2010) 3303–3312, https://doi.org/10.1016/j.actamat.2010.02.004.

[34] H. Beladi, Q. Chao, G.S. Rohrer, Variant selection and intervariant crystallographic planes distribution in martensite in a Ti–6Al–4V alloy, Acta Mater. 80 (2014) 478–489, https://doi.org/10.1016/j.actamat.2014.06.064.

[35] C. Cai, X. Wu, W. Liu, W. Zhu, H. Chen, J.C.D. Qiu, C.-N. Sun, J. Liu, Q. Wei, Y. Shi, Selective laser melting of near-α titanium alloy Ti-6Al-2Zr-1Mo-1V: parameter optimization, heat treatment and mechanical performance, J. Mater. Sci. Technol. 57 (2020) 51–64, https://doi.org/10.1016/j.jmst.2020.05.004.

[36] H. Attar, S. Ehtemam-Haghighi, D. Kent, I.V. Okulov, H. Wendrock, M. Bönisch, A.S. Volegov, M. Calin, J. Eckert, M.S. Dargusch, Nanoindentation and wear properties of Ti and Ti-TiB composite materials produced by selective laser melting, Mater. Sci. Eng., A 688 (2017) 20–26, https://doi.org/10.1016/j.msea.2017.01.096.

[37] D. Liu, S.Q. Zhang, A. Li, H.M. Wang, Microstructure and tensile properties of laser melting deposited TiC/TA15 titanium matrix composites, J. Mater. Sci. Technol. 485 (2009) 156–162, https://doi.org/10.1016/j.jallcom.2009.05.112.

[38] Q. Yan, B. Chen, J.S. Li, Super-high-strength graphene/titanium composites fabricated by selective laser melting, Carbon 174 (2021) 451–462, https://doi.org/10.1016/j.carbon.2020.12.047.

[39] H.Q. Liu, M.H. Fang, Y.F. Han, G.F. Huang, Z.G. Sun, L. Zhang, W.J. Lu, Achieving strength-ductility combination and anisotropy elimination in additively manufactured TiB/Ti6Al4V by *in situ* synthesized network architecture with fine grains, Composites, Part B 262 (2023) 110822, https://doi.org/10.1016/j.compositesb.2023.110822.

[40] S.H. Feng, Y.F. Han, C. Du, H.Q. Liu, F. Chen, J.W. Le, K. Wang, G.F. Huang, W.J. Lu, Dual hetero-structured Ti composites by manipulating self-assembled powder embedded with nano-reinforcements, Composites, Part B (2024) 111999, https://doi.org/10.1016/j.compositesb.2024.111999.

[41] T. DebRoy, H.L. Wei, J.S. Zuback, T. Mukherjee, J.W. Elmer, J.O. Milewski, A.M. Beese, A. Wilson-Heid, A. De, W. Zhang, Additive manufacturing of metallic components – process, structure and properties, Prog. Mater. Sci. 92 (2018) 112–224, https://doi.org/10.1016/j.pmatsci.2017.10.001.

[42] M. Elahinia, N. Shayesteh Moghaddam, M. Taheri Andani, A. Amerinatanzi, B.A. Bimber, R.F. Hamilton, Fabrication of NiTi through additive manufacturing: a review, Prog. Mater. Sci. 83 (2016) 630–663, https://doi.org/10.1016/j.pmatsci.2016.08.001.

[43] X. Liu, C. Zhao, X. Zhou, Z. Shen, W. Liu, Microstructure of selective laser melted AlSi10Mg alloy, Mater. Des. 168 (2019) 107677, https://doi.org/10.1016/j.matdes.2019.107677.

[44] E. Fereiduni, A. Ghasemi, M. Elbestawi, Microstructural characterization and mechanical properties of nano-scale/sub-micron TiB-reinforced titanium matrix composites fabricated by laser powder bed fusion, J. Mater. Sci. Technol. 896 (2022) 163054, https://doi.org/10.1016/j.jallcom.2021.163054.

[45] Y.B. Hu, W.L. Cong, X.L. Wang, Y.C. Li, F.D. Ning, H. Wang, Laser deposition-additive manufacturing of TiB-Ti composites with novel three-dimensional quasi-continuous network microstructure: effects on strengthening and toughening, Composites, Part B 133 (2018) 91–100, https://doi.org/10.1016/j.compositesb.2017.09.019.

[46] D. Pan, S.F. Li, L. Liu, X. Zhang, B. Li, B. Chen, M.Q. Chu, X.D. Hou, Z.G. Sun, J. Umeda, K. Kondoh, Enhanced strength and ductility of nano-TiBw-reinforced titanium matrix composites fabricated by electron beam powder bed fusion using Ti6Al4V–TiBw composite powder, Addit. Manuf. 50 (2022), https://doi.org/10.1016/j.addma.2021.102519.

[47] M. Wang, Y. Zhao, L.D. Wang, Y.P. Zhu, X.J. Wang, J. Sheng, Z.Y. Yang, H.L. Shi, Z.D. Shi, W.D. Fei, Achieving high strength and ductility in graphene/magnesium composite via an *in situ* reaction wetting process, Carbon 139 (2018) 954–963, https://doi.org/10.1016/j.carbon.2018.08.009.

[48] Z. Zhang, D.L. Chen, Consideration of Orowan strengthening effect in particulate-reinforced metal matrix nanocomposites: a model for predicting their yield strength, Scr. Mater. 54 (2006) 1321–1326, https://doi.org/10.1016/j.scriptamat.2005.12.017.

[49] H. Fukuda, T.W. Chou, A probabilistic theory of the strength of short-fiber composites with variable fibre length and orientation, J. Mater. Sci. 17 (1982) 1003–1011, https://doi.org/10.1007/bf00543519.

[50] A. Muiruri, M. Maringa, W. du Preez, Evaluation of dislocation densities in various microstructures of additively manufactured Ti6Al4V (Eli) by the method of X-ray diffraction, Materials 13 (2020) 5355, https://doi.org/10.3390/ma13235355.

[51] J.S. Keist, S. Nayir, T.A. Palmer, Impact of hot isostatic pressing on the mechanical and microstructural properties of additively manufactured Ti–6Al–4V fabricated using directed energy deposition, Mater. Sci. Eng., A 787 (2020), https://doi.org/10.1016/j.msea.2020.139454.